Integrated Experimental and Numerical Analysis of an Atmospheric Pressure Reactive Air Plasma Jet Generated by Dielectric Barrier Discharge

Hideya Nishiyama[1], Hidemasa Takana[1], Hirofumi Shimizu[2], Yoshihiko Iwabuchi[2] and Yoshikatsu Nakano[1]

[1]Institute of Fluid Science, Tohoku University, 2-1-1, Katahira, Aoba-ku, Sendai, 980-8577, Japan

[2]Graduate School of Engineering, Tohoku University, Sendai, 980-8579, Japan

E-mail: nishiyama@ifs.tohoku.ac.jp

Abstract

The effects of applied voltage, pulse frequency, flow rate and permittivity of dielectric material on the concentration of O_3 and NO_2 in a Dielectric Barrier Discharge (DBD) air plasma jet are experimentally investigated for industrial applications. Furthermore, the production and decay processes of chemical species and also time dependent chemical species concentration field in a DBD discharge region are numerically analyzed by integrated chemical reaction model with thermofluid flow field. There is a reasonable agreement of O_3 and NO_2 concentration with experimental data.

NOMENCLATURE

c	sound velocity m/s
C_p	specific heat at constant pressure J/(kg·K)
C_v	specific heat at constant volume J/(kg·K)
D	diffusion coefficient m^2/s
E	electric field strength kV/cm
E_t	stagnant internal energy J/m^3
f	pulsed frequency Hz
I	discharge current A
k	reaction rate constant m^3/s or m^6/s
N	total number density $(m^3)^{-1}$
n_s	number density of species $(m^3)^{-1}$
P_{in}	input electric power W
p	pressure Pa
Q_{air}	air flow rate Nℓ/min
r	radial coordinate mm
R	gas constant J/(kg·K)
t	time μs
T	gas temperature K
T_e	electric temperature K
u	velocity vector
u	axial velocity m/s
V_{pp}	applied voltage kV
v	radial velocity m/s
z	axial coordinate mm

Greek

γ	specific ratio

ε_0 permittivity of vacuum C/Vm
ε_r relative permittivity of dielectric material
η heat input efficiency
λ thermal conductivity W/(m·K)
μ viscous coefficient kg/(m·s)
ρ density kg/m^3
ρ_e charged density C
τ shear stress Pa
ϕ electric potential V
Φ_D viscous dissipation W/m^3
$\dot{\omega}_s$ production rate of species kg/(m^3·s)

1. INTRODUCTION

Recently, the plasma assisted combustion technology has been especially paid attention in the performance of aerospace jet engine and automobile engine [1-4]. It has been elucidated by previous study that ozone, oxygen radical, NOx and hydrogen-monoxide in a plasma mainly play important roles for lean combustion enhancement and reduction of ignition delay [5]. Furthermore, ozone has been extensively used for industrial and environmental applications such as oxidizing process for material, soot suppression, NOx removal from exhaust gas, bleaching, sterilization and deodorization. In these industrial applications [6,7], it is very important to produce many reactive radicals under the small input power conditions. However, there are a few investigations on reactive air jet analysis under the small input power conditions [8,9] so far. Among various kind of discharges, dielectric barrier discharge (DBD) is expected to be effective method to produce many radicals under applying pulsed high voltage.

In the present study, the downstream concentration field of produced reactive species and gas temperature in an air jet discharged by DBD are experimentally investigated for various operating conditions such as applied voltage, frequency, supplied air flow rate and dielectric material of electrode. Furthermore, time evolution of production and decay process of chemical species is numerically analyzed in the discharge and downstream regions and is compared with experimental data.

2. EXPERIMENTAL ANALYSIS

2.1 Experimental Apparatus and Measurement

Figure 1 shows the schematic illustration of experimental apparatus, which consists of pulsed power supply, coaxial DBD air plasma torch and compressed air cylinder. The electrodes are made of copper, inner electrode is applied with high voltage and outer electrode is grounded respectively, of which

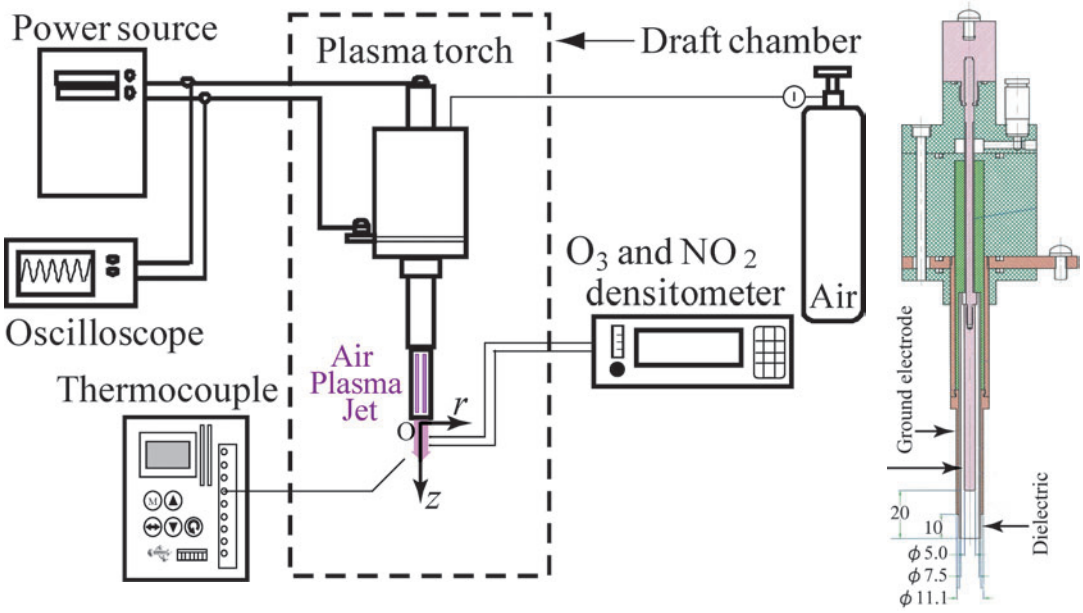

Figure 1. Schematic illustration of experimental apparatus

annular gap is 1.25 mm. Inner surface of ground electrode is covered with three kinds of dielectric materials of either quartz glass, alumina or zirconia of which thickness is 0.8 mm.

The applied sinusoidal voltage is from 9 kV - 36 kV_{pp} with frequency from 0.1 kHz to 5.0 kHz. The working gas is industrial dried air and its flow rate is controlled 1.5 Nℓ/min - 9.0 Nℓ/min. The surrounding gas is air at room temperature and atmospheric pressure. The produced radicals and other chemical species in the air flow are measured by concentration meter (SEKI electronics, SOZ-3503A and HODAKA, HT-2000) at 10, 20, 30 mm downstream from a torch exit under the assumption of chemically frozen flow during the sampling. The temperature is also measured by thermocouple at the same locations.

2.2 Experimental Results and Discussion

Figure 2 shows the pictures of air plasma jet generated by DBD discharge for various applied frequencies with the applied voltage of 28 kV under the flow rate of 6.0 Nℓ/min. The radiation intensity from nitrogen molecule increases and discharge extends to the downstream with increasing applied frequency. Although it is not shown in the figure, air plasma does not elongate with increase in flow rate under the constant applied voltage and sinusoidal frequency. This is because of the decrease in the specific input energy with increasing gas flow rate.

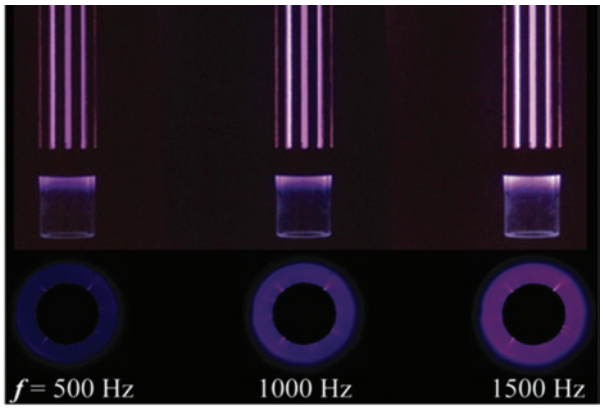

V_{pp} = 28 kV, Q = 6.0 N/min

Figure 2. Pictures of DBD air plasma jet with applied frequency

Figures 3 and 4 show the ozone concentration as functions of applied voltage and frequency for various dielectric materials and air flow rate. Ozone concentration is measured by ozone densitometer at the location of z = 10 mm. Ozone concentration increases linearly both for applied voltage and frequency due to the active electron impact. This results show the high controllability of ozone production by both applied voltage and frequency. Higher ozone concentration can be produced for alumina with permittivity of 9.7 compared with quarts glass of 3.8 at the same applied voltage. This is because of many electrons production with higher electric field for electron impact to produce ozone for alumina. On the other hand, the ozone concentration decreases with air gas flow rate at the same applied voltage due to the ozone dilution.

Figure 5 shows the ozone concentration as a function of specific input energy. It is clearly seen that there is an optimum value of specific input energy to obtain maximum ozone concentration for alumina and quartz. Highest ozone can be produced with smaller specific input power for alumina. However, higher ozone concentration cannot be obtained for zirconia with highest permittivity of 33 and tan δ of 16.0×10^{-4} (at 1MHz) among other dielectrics (tan δ = 1.0 for quartz and 2.0 for alumina, both at 1 MHz), because of the instability of DBD plasma generation with the large dielectric heat loss.

Figure 6 shows the radial distribution of ozone and nitrogen dioxide in the downstream. Ozone concentration is about two times higher than nitrogen dioxide and its gradient is steep between electrode gap. On the other hand, nitrogen dioxide shows plateau distribution in a core region. This comes from the different chemical reaction processes with other species in entrained surrounding air and diffusion coefficient of ozone and nitrogen dioxide in radial direction.

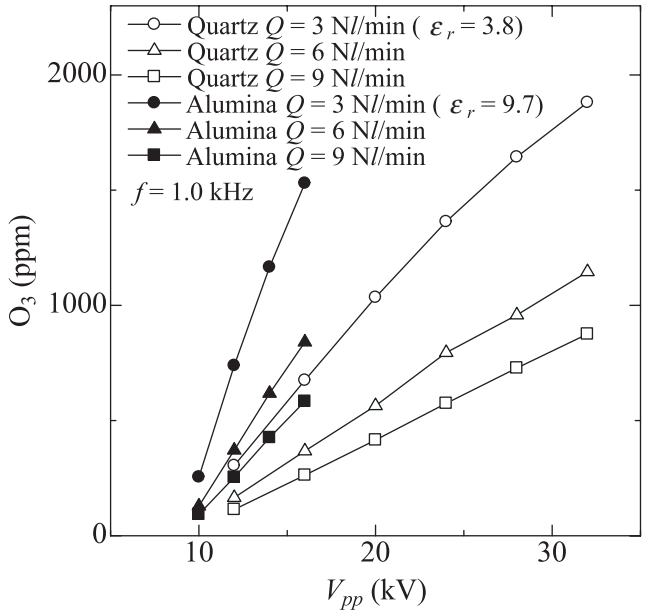

Figure 3. Ozone concentration with applied voltage

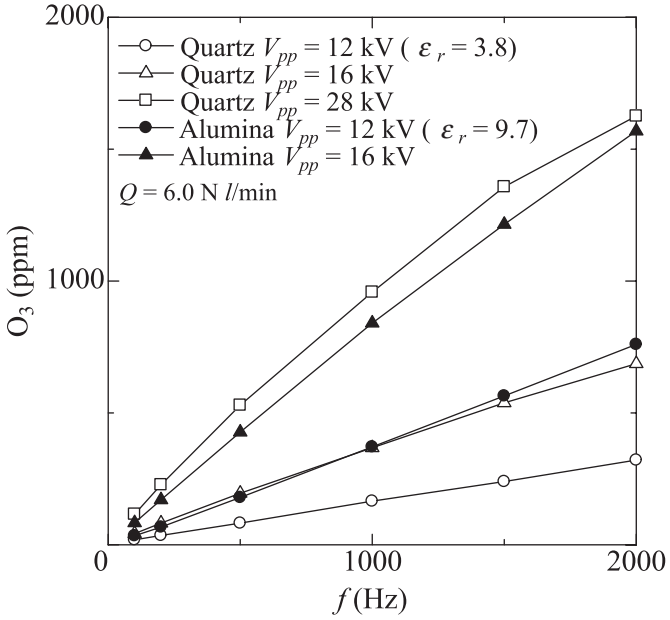

Figure 4. Ozone concentration with applied frequency

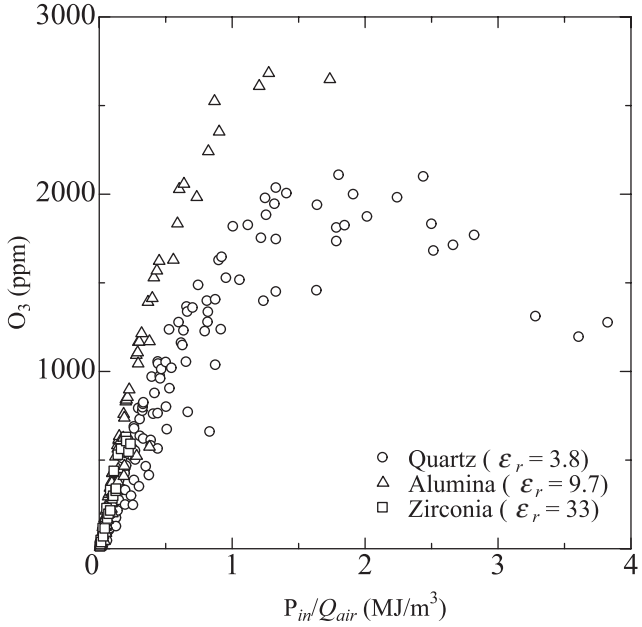

Figure 5. Ozone concentration with specific input energy

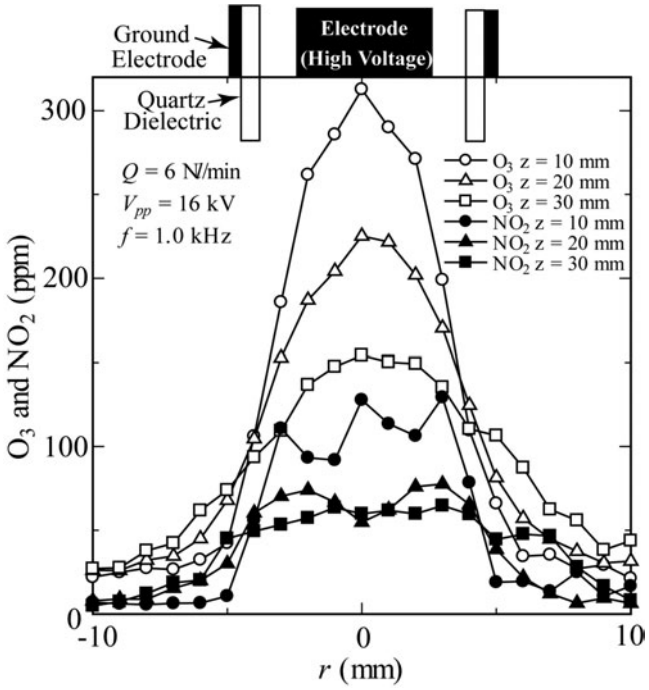

Figure 6. Radial distributions of ozone and nitrogen dioxide

Figure 7 shows the radial temperature distribution in the downstream. The distribution shows nearly symmetry. The temperature is nearly 330 K in the core at z = 10 mm, although DBD jet is nothermal plasma. This may result in the suppression of effective ozone generation.

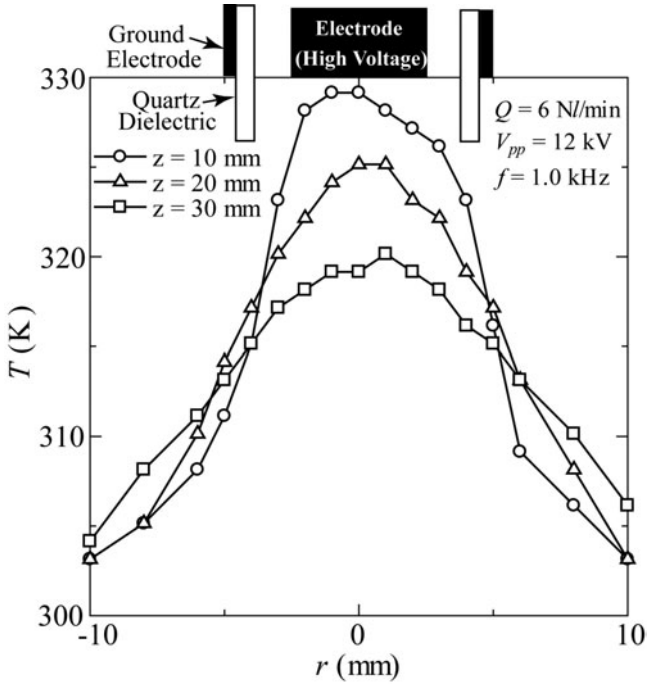

Figure 7. Radial distributions of gas temperature

3. NUMERICAL ANALYSIS

3.1 Governing Equations

Figure 8 shows a schematic illustration of computational domain and boundary conditions referring to experimental apparatus as shown in Fig.1. The electron impact process by application of high voltage is the dominant chemical reaction which produces various kinds of activated radicals in the air. Kossyi proposed about 300 chemical reaction equations for non-equilibrium air plasma [10]. However, it is important to reduce the number of equations for complex chemical reactions to reduce computational time. Thus, the simplified reaction model by Benilov [11] is adopted to clarify the chemical species

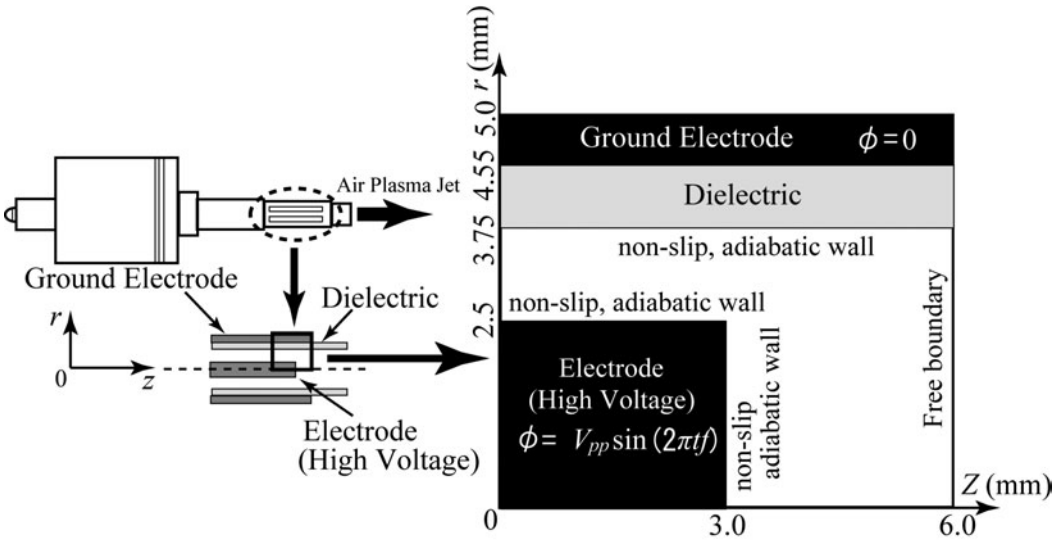

Figure 8. Schematic illustration of computational domain and boundary conditions

production processes in a discharge region. To derive the governing equation, the following assumptions are introduced here.

1. Thermofluid field is turbulent and axisymmetrical 2D.
2. Plasma is regarded as a continuous and compressible flow.
3. Plasma is nonequilibrium.
4. Electron temperature is given as a function of E/N.
5. Radiation is ignored.
6. Composition of air as a working gas is 80 % of nitrogen and 20 % of oxygen.
7. It is assumed that $10^9/m^3$ of electrons exists by the cosmic ray before discharge.
8. Streamer structure in DBD is not considered.

The governing equations are described as follows [12]:

Mass conservation equation

$$\frac{\partial \rho}{\partial t} + \nabla \cdot (\rho \mathbf{u}) = 0, \quad \rho = \sum_{s=1}^{n} \rho_s, \quad \rho_s = m_s n_s \tag{1}$$

Momentum conservation equation

$$\frac{\partial}{\partial t}(\rho \mathbf{u}) + \nabla \cdot (\rho \mathbf{u}\mathbf{u}) = -\nabla p + \nabla \cdot \tau + \sum_{s=1}^{n} n_s e Z_s \mathbf{E} \tag{2}$$

Energy conservation equation

$$\frac{\partial E_t}{\partial t} + \nabla \cdot \left((E_t + p)\mathbf{u} \right) = \nabla \cdot (\lambda \nabla T) + \nabla \cdot (\mathbf{u} \cdot \tau) + \sum_{s=1}^{n} n_s e Z_s \mathbf{E} \cdot \mathbf{u}_s \tag{3}$$

$$E_t = \sum_{s \neq e}^{n} \rho_s c_{vs} T + \frac{1}{2} \rho \mathbf{u}\mathbf{u} \tag{4}$$

where electron temperature is given by [12]

$$\begin{aligned} T_e &= 0.447 \left(\frac{E}{N} \right)^{0.16} \quad \text{at} \quad \frac{E}{N} < 50, \\ T_e &= 0.0167 \left(\frac{E}{N} \right) \quad \text{at} \quad \frac{E}{N} > 50 \ . \end{aligned} \tag{5}$$

Mass conservation equations of chemical species

$$\begin{aligned} &\frac{\partial \rho_s}{\partial t} + \nabla \cdot (\rho_s \mathbf{u}_s) = \dot{\omega}_s, \\ &\mathbf{u}_s = \mathbf{u} + \mathbf{v}_s \end{aligned} \tag{6}$$

where drift velocity is as follows:

$$\begin{aligned} \mathbf{v}_n &= -D_n \frac{\nabla \rho_n}{\rho_n}, \\ \mathbf{v}_i &= -D_{ion} \frac{\nabla \rho_{ion}}{\rho_{ion}} + \mu_{ion} \mathbf{E}, \\ \mathbf{v}_e &= -D_e \frac{\nabla \rho_e}{\rho_e} - \mu_e \mathbf{E} \end{aligned} \tag{7}$$

Equation of state

$$p = \sum_{s \neq e}^{n} p_s = \sum_{s \neq e}^{n} \rho_s \frac{R}{M_s} T \tag{8}$$

Poisson equation

$$\nabla \cdot (\varepsilon_r \nabla \varphi) = -\frac{\rho_c}{\varepsilon_0} \tag{9}$$

The electron impacts as a function of electron temperature derived from eq. (5) are the predominant processes for the radical production in the DBD. The reaction coefficients for electron impact reactions are described as a function of *E*/*N*. The subscription *s* in the above equations means 19 chemical species (N_2, O_2, O_3, N, O, NO, NO_2, N_2^+, N^+, O_2^+, O^+, NO^+, NO_2^+, O^-, O_2^-, O_3^-, NO^-, NO_2^-, *e*). Based on the chemical reaction model proposed by Kossyi [10] and Benilov [11], the 89 chemical reactions in the air plasma jet are considered for simplicity as shown in table 1.

Table 1. Chemical reactions and their rate coefficients included in the model

Number	Reaction	Rate constant (m^3/s, m^6/s)	Ref.
1	$O_3 + e \rightarrow O_2 + O + e$	$1.0\times10^{-5}\times\exp(-24.7\text{-}422/(E/N))$	11
2	$NO_2^+ + e \rightarrow NO + O$	$2.0\times10^{-13}\times(300/T_e)^{0.5}$	11
3	$N_2^+ + e \rightarrow N + N$	$2.8\times10^{-13}\times(300/T_e)^{0.5}$	11
4	$O_2^+ + e \rightarrow O + O$	$2.0\times10^{-13}\times(300/T_e)$	11
5	$NO^+ + e \rightarrow N + O$	$4.0\times10^{-13}\times(300/T_e)^{1.5}$	11
6	$e + e + A^+ \rightarrow e + A$ $A = N_2, O_2, NO, N, O$	$1.0\times10^{-31}\times(300/T_e)^{4.5}$	11
7	$e + A^+ + M \rightarrow A + M$ $A = N_2, O_2, NO, N, O$ $M = N_2, O_2$	$6.0\times10^{-39}\times(300/T_e)^{1.5}$	11
8	$e + O_2 + O_2 \rightarrow O_2^- + O_2$	$1.4\times10^{-41}\times(300/T_e)\times\exp(-600/T)\times\exp(700(T_e\text{-}T)/T_e/T)$	11
9	$e + O_2 + N_2 \rightarrow O_2^- + N_2$	$1.07\times10^{-43}\times(300/T_e)^2\times\exp(-70/T)\times\exp(1100(T_e\text{-}T)/T_e/T)$	11
10	$e + O + O_2 \rightarrow O^- + O_2$	1.0×10^{-43}	11
11	$e + O + O_2 \rightarrow O + O_2^-$	1.0×10^{-43}	11
12	$e + O_3 \rightarrow O_2^- + O$	1.0×10^{-15}	11
13	$e + O_3 \rightarrow O^- + O_2$	1.0×10^{-17}	11
14	$e + NO_2 \rightarrow NO_2^-$	3.0×10^{-17}	11
11	$e + NO + M \rightarrow NO^- + M$ $M = N_2, O_2$	1.0×10^{-42}	11
16	$e + NO_2 \rightarrow O^- + NO$	1.0×10^{-17}	11
17	$O_2^- + N_2 \rightarrow O_2 + N_2 + e$	$1.9\times10^{-18}\times(300/T_e)^{0.5}\times\exp(-4990/T)$	11
18	$O_2^- + O_2 \rightarrow O_2 + O_2 + e$	$2.7\times10^{-16}\times(300/T_e)^{0.5}\times\exp(-5590/T)$	11
19	$O_2^- + O \rightarrow O_3 + e$	1.5×10^{-16}	11
20	$O_2^- + N \rightarrow NO_2 + e$	5.0×10^{-16}	11
21	$O^- + O \rightarrow O_2 + e$	5.0×10^{-16}	11
22	$O^- + N \rightarrow NO + e$	2.6×10^{-16}	11
23	$O_3^- + O \rightarrow O_2 + O_2 + e$	3.0×10^{-16}	11
24	$O^- + O_2 \rightarrow O_3 + e$	5.0×10^{-21}	11
25	$O^- + NO \rightarrow NO_2 + e$	2.1×10^{-16} 11	
26	$N + O_2 \rightarrow NO + O$	$1.1\times10^{-20}\times T\times\exp(-3150/T)$	11
27	$N + O_3 \rightarrow NO + O_2$	2.0×10^{-22}	11
28	$N + NO \rightarrow N_2 + O$	$1.05\times10^{-18}\times T^{0.5}$	11
29	$N + NO_2 \rightarrow N_2 + O_2$	7.0×10^{-19}	11
30	$N + NO_2 \rightarrow N_2 + O + O$	9.1×10^{-19}	11
31	$N + NO_2 \rightarrow NO + NO$	2.3×10^{-18}	11
32	$O + NO_2 \rightarrow NO + O_2$	$1.13\times10^{-17}\times(T/1000)^{0.18}$	11
33	$O + O_3 \rightarrow O_2 + O_2$	$2.0\times10^{-17}\times\exp(-2300/T)$	11
34	$NO + O_3 \rightarrow O_2 + NO_2$	$4.3\times10^{-18}\times\exp(-1560/T)$	11
35	$N + O + M \rightarrow NO + M$ $M = N_2, O_2$	$1.76\times10^{-43}\times T^{-0.5}$	11
36	$O + O_2 + N_2 \rightarrow O_3 + N_2$	$6.2\times10^{-46}\times(300/T)^2$	11
37	$O + O_2 + O_2 \rightarrow O_3 + O_2$	$6.9\times10^{-46}\times(300/T)^{1.25}$	11
38	$N^+ + O + M \rightarrow NO^+ + M$ $M = N_2, O_2$	1.0×10^{-41}	11
39	$N^+ + N + M \rightarrow N_2^+ + M$ $M = N_2, O_2$	1.0×10^{-41}	11

Number	Reaction	Rate constant (m^3/s, m^6/s)	Ref.
40	$O^+ + N_2 + M \rightarrow NO^+ + N + M$ $M = N_2, O_2$	$6.0\times10^{-41}\times(300/T)^2$	11
41	$O^+ + O + M \rightarrow O_2^+ + M$ $M = N_2, O_2$	1.0×10^{-41}	11
42	$O^+ + N + M \rightarrow NO^+ + M$ $M = N_2, O_2$	1.0×10^{-41}	11
43	$N^+ + O_2 \rightarrow O_2^+ + N$	2.8×10^{-16}	11
44	$N^+ + O_2 \rightarrow NO^+ + O$	2.5×10^{-16}	11
45	$N^+ + O_2 \rightarrow O^+ + NO$	2.8×10^{-17}	11
46	$N^+ + O \rightarrow N + O^+$	1.0×10^{-18}	11
47	$N^+ + O_3 \rightarrow NO^+ + O_2$	5.0×10^{-16}	11
48	$N^+ + NO \rightarrow N + NO^+$	8.0×10^{-16}	11
49	$N^+ + NO \rightarrow N_2^+ + O$	3.0×10^{-18}	11
50	$N^+ + NO \rightarrow O^+ + N_2$	1.0×10^{-18}	11
51	$O^+ + N_2 \rightarrow NO^+ + N$	$3.0\times10^{-18}\times\exp(-0.00311\times T)$	11
52	$O^+ + O_2 \rightarrow O_2^+ + O$	$3.3\times10^{-17}\times\exp(-0.00169\times T)$	11
53	$O^+ + O_3 \rightarrow O_2^+ + O_2$	1.0×10^{-16}	11
54	$O^+ + NO \rightarrow NO^+ + O$	2.4×10^{-17}	11
55	$O^+ + NO \rightarrow O_2^+ + N$	3.0×10^{-18}	11
56	$O^+ + NO_2 \rightarrow NO_2^+ + O$	1.6×10^{-15}	11
57	$N_2^+ + O_2 \rightarrow O_2^+ + N_2$	$6.0\times10^{-17}\times(300/T)^{0.5}$	11
58	$N_2^+ + O \rightarrow NO^+ + N$	$1.3\times10^{-16}\times(300/T)^{0.5}$	11
59	$N_2^+ + O \rightarrow O^+ + N_2$	$1.0\times10^{-17}\times(300/T)^{0.2}$	11
60	$N_2^+ + O_3 \rightarrow O_2^+ + O + N_2$	1.0×10^{-16}	11
61	$N_2^+ + N \rightarrow N^+ + N_2$	$2.4\times10^{-21}\times T$	11
62	$N_2^+ + NO \rightarrow NO^+ + N_2$	3.3×10^{-16}	11
63	$O_2^+ + N_2 \rightarrow NO^+ + NO$	1.0×10^{-23}	11
64	$O_2^+ + N \rightarrow NO^+ + O$	1.2×10^{-16}	11
65	$O_2^+ + NO \rightarrow NO^+ + O_2$	4.4×10^{-16}	11
66	$O_2^+ + NO_2 \rightarrow NO^+ + O_3$	1.0×10^{-17}	11
67	$O_2^+ + NO_2 \rightarrow NO_2^+ + O_2$	6.6×10^{-16}	11
68	$NO^+ + O_3 \rightarrow NO_2^+ + O_2$	1.0×10^{-21}	11
69	$NO_2^+ + NO \rightarrow NO^+ + NO_2$	2.9×10^{-16}	11
70	$O^- + O_2 + M \rightarrow O_3^- + M$ $M = N_2, O_2$	$1.1\times10^{-42}\times(300/T)$	11
71	$O^- + NO + M \rightarrow NO_2^- + M$ $M = N_2, O_2$	1.0×10^{-41}	11
72	$O_2^- + O \rightarrow O_2 + O^-$	3.3×10^{-16}	11
73	$O_2^- + O_3 \rightarrow O_2 + O_3^-$	4.0×10^{-16}	11
74	$O_2^- + NO_2 \rightarrow NO_2^- + O_2$	8.0×10^{-16}	11
75	$O^- + O_3 \rightarrow O + O_3^-$	5.3×10^{-16}	11
76	$O^- + NO_2 \rightarrow NO_2^- + O$	1.2×10^{-15}	11
77	$O_3^- + O \rightarrow O_2^- + O_2$	3.2×10^{-16}	11
78	$O_3^- + NO \rightarrow NO_2^- + O_2$	2.6×10^{-18}	11
79	$O_3^- + NO_2 \rightarrow NO_2^- + O_3$	7.0×10^{-16}	11
80	$NO^- + O_2 \rightarrow O_2^- + NO$	5.0×10^{-16}	11
81	$NO^- + NO_2 \rightarrow NO_2^- + NO$	7.4×10^{-22}	11
82	$A^- + B^+ \rightarrow A + B$ $A = O_2, O, O_3, NO, NO_2$ $B = N_2, O_2, N, O, NO, NO_2$	$2.0\times10^{-13}\times(300/T)^{0.5}$	11
83	$A^- + B^+ + M \rightarrow A + B + M$ $M = N_2, O_2$ $A = O_2, O$ $B = N_2, O_2, N, O, NO$	$2.0\times10^{-37}\times(300/T)^{2.5}$	11

Number	Reaction	Rate constant (m^3/s, m^6/s)	Ref.
84	$A^- + B^+ + M \rightarrow AB + M$ $M = N_2, O_2$ $A = O_2, O$ $B = N_2, O_2, N, O, NO$	$2.0\times10^{-37}\times(300/T)^{2.5}$	11
85	$e + O_2 \rightarrow O^- + O$	$3.3\times10^{-17}\times(E/N)^{0.8}\times\exp(-1.05\|5.3-\ln(E/N)\|^3)F$	12
86	$e + N_2 \rightarrow e + N + N$	$5.0\times10^{-15}\times\exp(-646/(E/N))F$	12
87	$e + O_2 \rightarrow e + O + O$	$1.7\times10^{-14}\times\exp(-324/(E/N))F$	12
88	$e + N_2 \rightarrow e + e + N_2^+$	$8.1\times10^{-15}\times\exp(-925/(E/N))F$	12
89	$e + O_2 \rightarrow e + e + O_2^+$	$4.9\times10^{-15}\times\exp(-657/(E/N))F$	12
		$F = \exp(\ 6.5\times10^3/(E/N)^2\times\exp(-0.29/(kT))\ )$	

3.2 Boundary Conditions

The boundary conditions for thermofluid field are summarized below.

Inlet: $T = 300$ K, $\dfrac{\partial\rho}{\partial z} = \dfrac{\partial\rho_s}{\partial z} = 0$, $u = 4.0$ m/s, $v = 0$, $\dfrac{\partial\phi}{\partial z} = 0$

Symetric axis: $\dfrac{\partial\rho}{\partial r} = \dfrac{\partial\rho_s}{\partial r} = 0$, $\dfrac{\partial p}{\partial r} = 0$, $\dfrac{\partial u}{\partial r} = v = 0$, $\dfrac{\partial\phi}{\partial r} = 0$

Wall: $T = 300$ K, $\dfrac{\partial\rho}{\partial n} = \dfrac{\partial\rho_s}{\partial n} = 0$, $u = v = 0$, $\dfrac{\partial\phi}{\partial n} = 0$

Outlet: $\dfrac{\partial\rho}{\partial z} = \dfrac{\partial\rho_s}{\partial z} = 0, \dfrac{\partial p}{\partial z} = 0, \dfrac{\partial u}{\partial z} = \dfrac{\partial v}{\partial z} = 0, \dfrac{\partial\phi}{\partial z} = 0$

The electrical potential ϕ_b on the surface of quartz glass is given as follows to satisfy the conservation of dielectric flux density between air and quartz glass:

$$\phi_b = \frac{\varepsilon_{air}\phi_{air}\Delta r_q + \varepsilon_q\phi_q\Delta r_{air}}{\varepsilon_{air}\Delta r_q + \varepsilon_q\Delta r_{air}} \tag{10}$$

where Δr_{air} and Δr_q are the space between the neighboring grid points in r-direction from the surface of quartz glass. ε_{air} and ε_q represent the relative permittivity of air and quartz glass, respectively. ϕ_{air} and ϕ_q show the neighboring electrical potential in air and quartz glass, respectively.

3.3 Numerical Results and Discussion

Figures 9 (a)-(c) show the time evolution of concentration of chemical species and electric field intensity at 1.0 μs, 3.0 μs and 5.0 μs respectively after discharge initiation. The operating condition is $V_{pp} = 20$ kV, $f = 1.0$ kHz and $Q = 6$ Nℓ/min. The electric field intensity increases around the electrode edge, which results in the active electron impact process to produce many chemical species due to the electron concentration. At 5.0 μs all the species such as oxygen radical, ozone and nitrogen dioxide are produced in the whole electrode region corresponding to the considerable increase in electrons. However, the ozone produced near electrode edge is relatively smaller compared with other species due to the decomposition of ozone by many electrons. It is suggested that many chemical species can be produced easily for the sharp edged electrode with electron concentration.

Figure 10 shows the electron temperature in the electrode region at 5.0 μs after the discharge initiation. The maximum electron temperature is given as a function of E/N as shown in equation (5) and then the reaction coefficients for electron impact is calculated as shown in table 1. The distribution of electron temperature correlates well with that of electrical field intensity. The electron temperature is highest around the corner of electrode.

Figure 11 shows the axial velocity, radial velocity, gas temperature and density in the electrode region. Since the chemical reaction time scale is considerably smaller than that of thermofluid field, there is no relation between them within 5.0 μs. Axial velocity is higher in the electrode gap. The vortex appears around the electrode edge due to thermal expansion of gas flow. Gas temperature and density are nearly uniform in the electrode region.

Figure 12 shows comparisons of ozone and nitrogen dioxide axial concentration with experimental

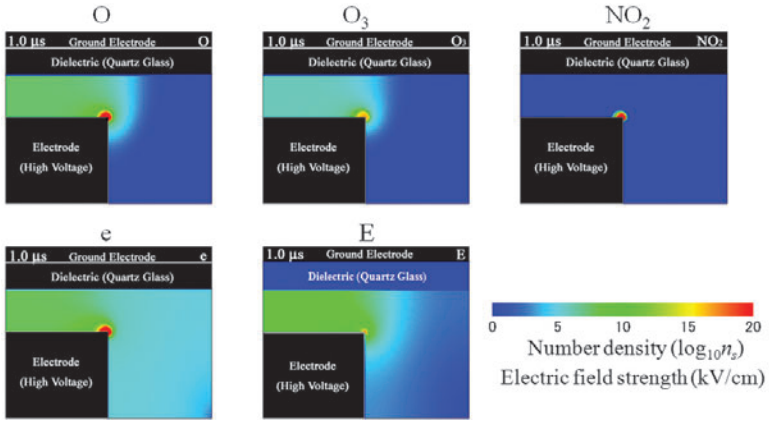

(a)

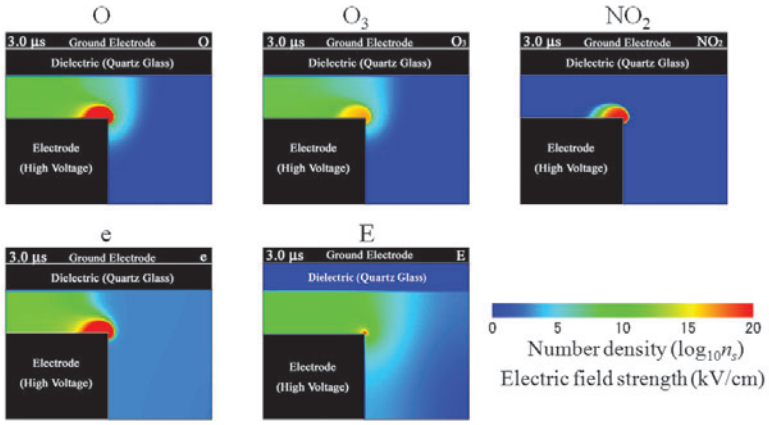

(b)

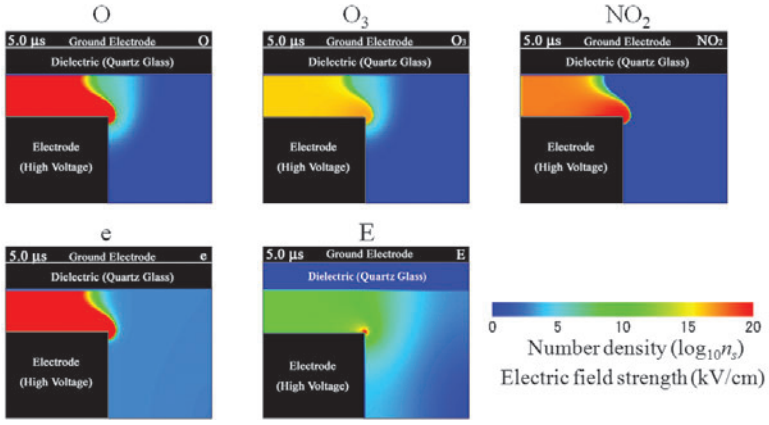

(c)

Figure 9. (a)-(c) Time evolution of chemical species concentration and electric field intensity

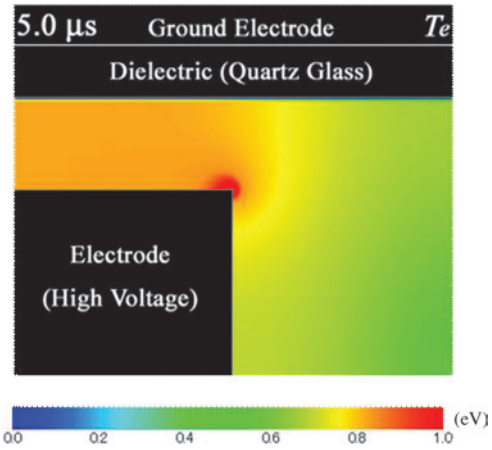

Figure 10. Electron temperature at 5.0 μs after the discharge ignition

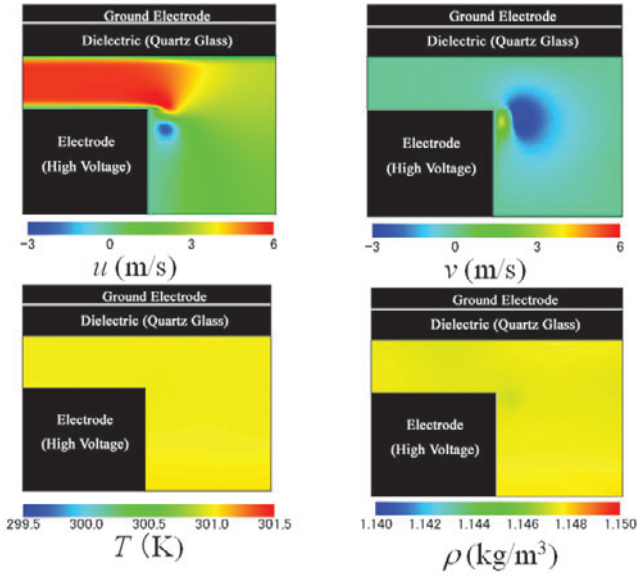

Figure 11. Axial velocity, radial velocity, gas temperature and density

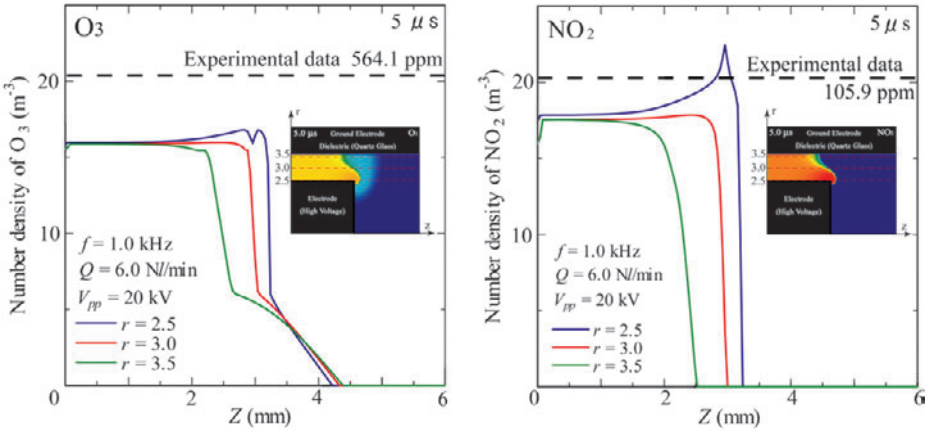

Figure 12. Comparisons of ozone and nitrogen dioxide concentrations with experiment

data, although simulation time of 5.0 μs is not sufficient for obtaining the steady state due to heavy computational loading. Experimental data shows the spatially averaged value. There is a reasonable agreement between them even before steady state of numerical simulation.

4. CONCLUSIONS

The integrated experimental and numerical analysis is conducted to clarify the radical production and decay processes, and their transport characteristics in an air DBD jet under various kinds of operating conditions. The obtained results are summarized as follows:

(1) The production of ozone increases linearly with applied voltage and frequency, which shows the high controllability. Highest concentration of ozone can be produced for alumina as a dielectric compared with quartz and zirconia.
(2) There is an optimum value of specific input energy to obtain the maximum ozone concentration. More than 2,500 ppm ozone can be produced by the smallest input power for alumina.
(3) Ozone concentration is higher than nitrogen dioxide in the downstream and their radial distribution is different each other due to the different chemical reactions and diffusion processes under the non-thermal condition.
(4) In the 2D numerical analysis, productions of oxygen radical, ozone, nitrogen dioxide and electron occur near electrode edge due to the concentration of a large number of produced electrons.
(5) All the chemical species increase considerably in the electrode channel due to the active electron impact process at 5.0 μs after discharge initiation. But ozone concentration is relatively smaller than that of other species due to ozone decomposition by other species in the discharge region.
(6) The numerical number densities of ozone and nitrogen dioxide show reasonable agreement with experimental data even for small discharge duration.

ACKNOWLEDGEMENTS

Authors would like to give our sincere thanks to Associate Professor T. Sato for his valuable discussions and technicians Mr. K. Katagiri, Mr. T. Nakajima and graduate student Mr. D. Furukawa for their supports in the experiment. The present work was partly supported by Grant-in-aid for Scientific Research (A) from Japan Society of Promotion of Science and the Global COE Program Grant of Flow Dynamics from the Ministry of Education, Culture, Sports, Science and Technology (2008-2012).

REFERENCES

[1] I. M. Vince, C. Vovelle and F. J. Weinberg, *The Effect of Plasma Jet Ignition on Flame Propagation and Sooting at the Rich Limit of Flammability*, Combustion and Flame, 1984, 56 (1), 105-112.

[2] B. N. Gangaly, *Plasma Assisted Improvement of High Speed High Altitude Aerospace Vehicle Design*, in: M. C. Bordage, A. Gleizes and J. J. Gonzalez, eds., Proceedings of the XV International Conference on Gas Discharges and Their Applications, Paul Sabatier Univ., Toulouse, 2004, 1017-1023.

[3] S. V. Pancheshnyi, D. A. Lacoste, A. Bourdon, and C. O. Laux, *Ignition of Propane–Air Mixtures by a Repetitively Pulsed Nanosecond Discharge*, IEEE Transactions on Plasma Science, 2006, 34 (6), 2478- 2487.

[4] S. Stange, Y. Kim, V. Ferreri, L. A. Rosocha and D. M. Coates, *Flame Images Indicating Combustion Enhancement by Dielectric Barrier Discharges*, IEEE Transactions on Plasma Science, 2005, 33 (2), 316- 317.

[5] T. Tachibana, K. Hirata, H. Nishida and H. Osada, *Effect of Ozone on Combustion of Compression Ignition Engines*, Combustion and Flame, 1991, 85 (3-4), 511-519.

[6] M. S. Cha, S. M. Lee, K. T. Kim and S. H. Chung, Soot Suppression by Nonthermal Plasma in Coflow Jet Diffusion Flames Using a Dielectric Barrier Discharge, Combustion and Flame, 2005, 141, 438-447.

[7] B. Eliasson, M. Hirth and U. Kogelschatz, Ozone synthesis from oxygen in dielectric barrier discharges, Journal of Physics D: Applied Physics, 1987, 20, 1421-1437.

[8] H. Nishiyama, H. Takana, S. Niikura, H. Shimizu, D. Furukawa, T. Nakajima, K. Katagiri and Y.

Nakano, *Characteristics of Ozone Jet Generated by Dielectric-Barrier Discharge*, IEEE Transactions on Plasma Science, 2008, 36 (4), 1328-1329.

[9] H. Nishiyama, K. Tsuri, H. Shimizu, K. Katagiri, H. Takana and Y. Nakano, *Activated Air Plasma Flow Generated by Pulsed Arc Discharge for Combustion Enhancement*, International Journal of Heat and Mass Transfer, 2009, 52 (7-8), 1778-1785.

[10] I. A. Kossyi, A. Y. Kostinsky, A. A. Matveyev and V. P. Silakov, *Kinetic Scheme of the Non-Equilibrium Discharge in Nitrogen-Oxygen Mixtures*, Plasma Sources Science and Technology, 1992, 1 (3), 207-220.

[11] M. S. Benilov and G. V. Naidis, *Modelling of Low-Current Discharges in Atmospheric-Pressure Air Taking Account of Non-Equilibrium Effects*, Journal of Physics D: Applied Physics, 2003, 36 (11), 1834- 1841.

[12] K. H. Becker, U. Kogelschatz, K. H. Schoenbach and R. J. Barker, *Non-Equilibrium Air Plasmas at Atmospheric Pressure*, Institute of Physics Publishing, London, 2005.